ORIGINAL PAPER-PRODUCTION ENGINEERING

Critical pressure (P_c) and critical temperature (T_c) of Midra shale

Mehdi Alipour[1] · A. Sakhaee-Pour[1]

Abstract
The critical pressure (P_c) and critical temperature (T_c) of shale gas depend on the characteristic pore size because of the importance of fluid–rock interactions in the matrix. This size dependency is neglected in highly permeable formations, where gas composition is only implemented because the fluid–fluid interactions are dominant. This study determines the critical properties by accounting for the characteristic pore size in the shale matrix and gas composition. The analyzed components are carbon dioxide, ethane, methane, n-butane, nitrogen, pentane, and propane. It shows that the bulk properties overestimate the actual critical properties. The overestimation varies between 15 and 26% in a uniform 5 nm conduit with a circular cross section, and it increases nonlinearly when decreasing the conduit size. Overestimation versus size is presented to provide a convenient tool for correcting the existing data. This study also determines the critical properties of Midra shale by accounting for the pore-throat size and pore-body size distributions. The former distribution is based on the mercury injection capillary pressure measurements of eight samples, whereas the latter is based on the nitrogen adsorption measurements of six samples. This study indicates that common bulk properties overestimate the critical properties of the studied shale between 5 and 22%. The results have applications in characterizing multiphase transport in shale gas reservoirs.

Keywords Shale gas · Critical pressure (P_c) · Critical temperature (T_c)

Introduction

The shale matrix is a nanofluidic system because its pore-throat and pore-body sizes are on the order of nanometers (Loucks et al. 2009; Milliken et al. 2013; Yu et al. 2018). Nanofluidics is a field study devoted to fluid transport in the sub-100 nm conduit (Eijkel and van den Berg, 2005; Tran and Sakhaee-Pour 2019). Because of the nanosize confinement, there are challenges in characterizing transport in shale. For instance, Singh and Singh (2011) indicated that the flow behavior changed significantly when the conduit was narrower than ten fluid molecules because they interacted with the boundary more than they did with each other. Their study underscores the importance of pore confinement for phase behavior based on the Monte Carlo simulation. Other researchers also stated that the phase equilibrium in nanosize pores deviated from the bulk behavior (Xiong et al. 2021; Zhao et al. 2021).

Because of the ultra-narrow conduits in the shale matrix, its transport properties differ from those of more permeable media. For instance, Li et al. (2016) reported that methane adsorption to the pore wall became important in determining transport in shale. Their molecular dynamics study shows that slippage and adsorption have competing effects on permeability, consistent with an earlier study in the literature (Sakhaee-Pour and Bryant 2012). Also, Song et al. (2018) proposed an analytical model based on fractal theory to estimate gas slippage in shale. Their findings, which agree with the study by Wang et al. (2017), suggest that the surface diffusion controls the gas transport where the conduit is narrower than 50 nm. Further, Wang et al. (2016) stated that velocity profiles became plug-like in the pressure-driven flow of octane and supercritical carbon dioxide in nanosized slits in the matrix. Moreover, Bai et al. (2019) emphasized the importance of accurately characterizing methane diffusion to understand shale gas transport. For this reason, they conducted a pressure pulse experiment to determine the effects of pore pressure on the diffusion coefficient, which was divided into three stages depending on the pore size.

Researchers have also studied the effects of thermal treatment on the shale pore structure. Chandra et al. (2023) used

✉ A. Sakhaee-Pour
asakhaee@central.uh.edu

1 Department of Petroleum Engineering, University of Houston, Houston, TX, USA

a high-resolution image, gas adsorption, small-angle X-ray, and neutron scattering to characterize the pore structure in oxic and anoxic environments heated up to 300°C. They indicated that heating formed new pores. In addition, Hazra et al. (2023) analyzed the effects of low-temperature combustion on the pore structure. Their low-pressure gas adsorptions confirmed that the pore structure changed significantly. More recently, Aruah et al. (2024) investigated the effects of thermal treatment on shale by interpreting its permeability from mercury injection capillary pressure measurements. They reported that the matrix permeability increased up to 20%, and there might be an optimum scenario for the enhancement that could be determined only experimentally.

Because of the importance of pore size in shale, researchers adopted different approaches to characterize it (Liu et al. 2022; Taghavinejad et al. 2020). For instance, Mastalerz et al. (2013) used mercury injection capillary pressure measurements to determine the pore-throat size distribution. Moreover, Clarkson et al. (2013) comprehensively analyzed shale formations using different techniques. They compared the results of small-angle and ultra-small-angle neutron scattering, low-pressure adsorption, and high-pressure mercury intrusion measurements on shale samples from North America. In addition, Zapata and Sakhaee-Pour (2016) employed nitrogen adsorption–desorption hysteresis to characterize the pore-body size distribution based on the acyclic model in which the spatial distribution of pore size is not random, and there is a single path between two points in the connected network of pore space (Sakhaee-Pour and Bryant 2015; Sakhaee-Pour and Li 2016). Further, two groups used scanning electron microscope images to explore the pore size (Deng et al. 2016; Liu et al. 2019) and provided detailed information about the shale samples. Further, Hazra et al. (2018a, b) characterized shale using low-pressure nitrogen adsorption–desorption experiments and concluded that a larger specific surface area corresponded to a higher thermal maturity in the studied shale.

Shale gas production has remained at an early stage in the Middle East, but there has been an increasing interest in unconventional hydrocarbon reservoirs in the region (Al-Shawaf et al. 2016; Al-Shamali et al. 2017). Cavelier (1970) was the first person to analyze the Qatari shale and describe its geology. More recently, Sahin (2013) assessed the potential of shale by exploring the Paleozoic sequence in the Middle East and reviewed the primary sources of unconventional gas to guide exploration activities. Also, Casey et al. (2015) presented an economic model for shale gas in Saudi Arabia to capture various phases of unconventional resource development. They adjusted the base model originally tested against a North American shale to calibrate for a specific field. Moreover, other researchers have explored the stratigraphy and fossil content of shale (Al-Saad 2005; Al-Saad and Sadooni 2011) without

assessing its potential as a hydrocarbon resource, unlike the recent study by Al-Saad et al. (2019) for the Unayzah formation. Al-Saad et al. (2019) collected twenty samples from three wells in the Dukhan field; many were of poor quality with low total organic carbon content. In addition, Alessa et al. (2021) evaluated the pore structure of Midra shale by analyzing mercury injection capillary pressure and nitrogen adsorption measurements. While their study reports the pore-throat and pore-body size distributions of the Midra shale, there is limited information about its transport properties.

This study determines the critical properties (P_c and T_c) of Midra shale. It first determines the critical properties of various gas components, such as methane, ethane, and propane, in a nanosize conduit by quantifying the error of using bulk properties instead of actual properties. It then quantifies the critical properties of the Midra shale by accounting for the effective pore-throat and pore-body sizes. The effective sizes are interpreted from core-scale measurements.

Studied shale

This study investigated shale samples from the Midra formation collected from the Dukhan Hills at Umm Bab in Qatar (Alessa et al. 2021, 2022). The Midra formation is a yellowish-brown and greenish-gray slate, and its consistency, color, and composition vary in the region. Its sediments are formed of thin, friable foliations and stained with pinkish and red colors because of the weathering of the iron contents in the upper sediments. Figure 1 shows examples of the studied shale.

Fig. 1 Examples of the studied shale

Method

The critical properties (P_c and T_c) of a gas are required for modeling its multiphase transport. They are used to estimate fundamental properties, such as gas density (ρ_g), formation volume factor (B_g), and viscosity (μ_g). The critical properties in a nanosize conduit deviate from the bulk properties in wider pores abundant in highly permeable formations. The deviations can be expressed as ratios as follows:

$$R_P = \frac{P_c \text{ (actual)}}{P_c \text{ (bulk)}} \tag{1}$$

$$R_T = \frac{T_c \text{ (actual)}}{T_c \text{ (bulk)}} \tag{2}$$

where R_P is the ratio of the critical pressure of gas in the nanosize conduit to the bulk property, P_c (actual) is the critical pressure in the nanosize conduit, P_c (bulk) is the critical pressure of the bulk volume, R_T is the ratio of the critical temperature of the gas in the nanosize conduit to the bulk value, T_c (actual) is the critical temperature in the nanosize conduit, and T_c (bulk) is the critical temperature pressure of the bulk volume.

There are different models for the ratios in the literature (Ma et al. 2013; Jin et al. 2013; Zarragoicoechea and Kuz 2002, 2004). This study used the model developed by Zarragoicoechea and Kuz (2002, 2004) because it is used widely (Teklu et al. 2014; Jin and Firoozabadi 2016; Tran and Sakhaee-Pour 2018; Jia et al. 2019). It expresses the ratios by accounting for the conduit size (d) and the Lennard–Jones coefficient (σ) as follows:

$$R_P = R_T = 1 - 1.882\frac{\sigma}{d} + 0.966\left(\frac{\sigma}{d}\right)^2 \tag{3}$$

Overestimations of critical properties in a nanosize conduit

The ratio of the critical properties (Eq. 3) is smaller than unity (Tran and Sakhaee-Pour 2018); thus, bulk properties overestimate the actual properties, and the overestimation is determined as follows:

$$\text{Overestimation(\%)} = \frac{\left[\text{bulk property} - \text{actual property}\right]}{\text{actual property}}$$
$$\times 100 = [\frac{1}{R_p} - 1] \times 100 \tag{4}$$

There is no compositional analysis of the shale because its hydrocarbon is not produced. Hence, this study used the average composition of a shale formation in the literature (Korpys et al. 2014). The Lennard–Jones coefficients of the components were also based on the public data in the literature (Smoot, 1979; Tchouar et al. 2003). Table 1 lists the pertinent properties.

Next, we turn to the actual critical properties by determining how bulk properties overestimate them. The determination is carried out for conduits narrower than 30 nm. Figure 2 shows that the overestimation increases monotonically with decreasing size and becomes important where the conduit size is smaller than 10 nm. Although overestimation is observed in all components, it is the least significant for methane. Thus, the error of using standard bulk properties decreases when the volume fraction of methane increases.

The minimum difference between the actual and bulk properties of methane is consistent with its Lennard–Jones coefficient, the smallest coefficient in Table 1. The coefficient is the distance at which the intermolecular potential between two nonbonding particles is zero, and it provides a measure of the distance between the two. The higher overestimations of the actual properties of heavier and larger components, such as pentane, are also reasonable because a smaller number of larger molecules fill the uniform nanosize conduit with a circular cross section. Thus, they behave more differently than their bulk.

The plotted overestimations provide a convenient tool for estimating the error of using bulk properties in the matrix. For such estimations, the characteristic pore size should be implemented. For instance, if the characteristic pore size is close to 5 nm, bulk properties overestimate the actual properties between 15 and 26%. The overestimation varies from 28 to 48% if the size is close to 3 nm. Obviously, the lower overestimation corresponds to smaller molecules.

Table 1 Bulk properties of various components and gas composition

	σ (nm)	T_c (K)	P_c (psi)	Volume (fraction)
Carbon dioxide	0.3941	304	1072	0.005
Ethane	0.444	305.4	708.0	0.027
Methane	0.376	190.4	673.3	0.943
n-Butane	0.469	425.2	550.4	0.002
Nitrogen	0.380	126.2	492.4	0.015
Pentane	0.578	469.6	488.8	0.002
Propane	0.512	369.9	617.4	0.006

Fig. 2 Overestimation of the actual critical property (P_c or T_c) of gas with the conduit size when bulk properties are used
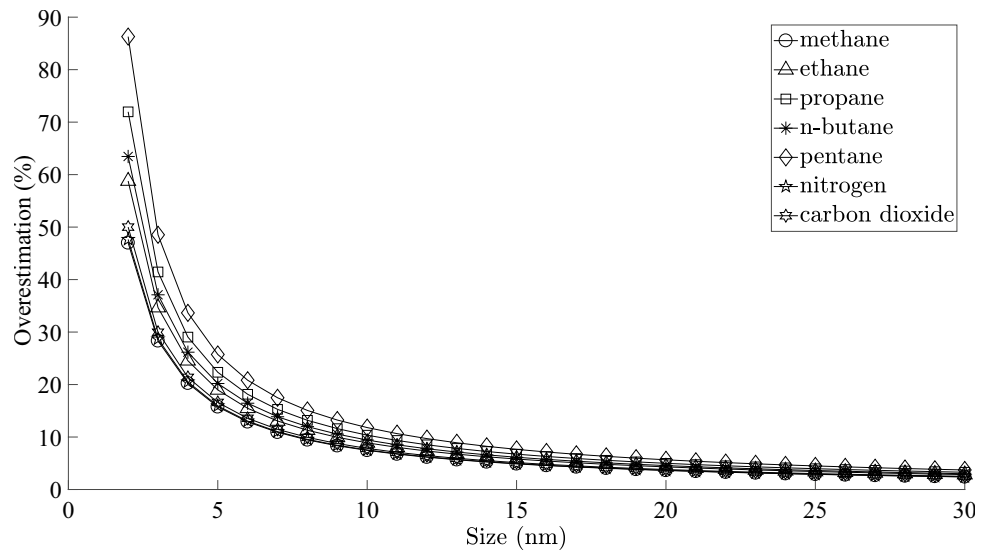
Natural nanofluidic system in the shale matrix

The pore space in the shale matrix is a nanofluidic system because its characteristic size is on the order of nanometers. In contrast with the synthetic nanofluidic system, it has a complex topology that makes its characterization challenging. This study used mercury injection and nitrogen adsorption measurements to probe the effective sizes at the core scale.

Mercury injection capillary pressure measurements

Mercury was injected into the sample to measure its capillary pressure because mercury does not react with rock, and it is a nonwetting phase to the rock. The capillary pressure required for intrusion determines the pore-throat size. The characteristic size of a single conduit is determined by the Young–Laplace equation as follows:

$$d = \frac{4\,\gamma\,\cos(\theta)}{p_{capillary}} \tag{5}$$

where d is the conduit diameter, γ is the interfacial tension, θ is the contact angle, and $p_{capillary}$ is the capillary pressure. The mercury saturation in the sample is determined by normalizing the injected volume, and it specifies the wetting phase saturation as follows:

$$S_w = 1 - S_{Hg} = 1 - V_{Hg}\big(p_{capillary}\big)/V_{Hg}(\text{max}) \tag{6}$$

where S_w is the wetting phase saturation, S_{Hg} is the mercury saturation, $V_{Hg}\big(p_{capillary}\big)$ is the mercury volume in the sample at a given capillary pressure, and $V_{Hg}(\text{max})$ is the maximum volume of the injected mercury.

This study used eight shale samples to characterize the capillary pressure (Fig. 3). Samples 1–8 were 0.7971, 0.5940, 1.1240, 0.6216, 1.0076, 0.6687, 0.6538, and 0.6439 g, respectively, and they were heated to 100 °C to remove moisture and left to reach room temperature. Their shapes were irregular, and they were placed in an empty cell invaded by mercury. The raw measurements exhibited unrealistic intrusion at low capillary pressures corresponding to filling the empty cell and closing cracks. Thus, the raw measurements were corrected by discarding the mercury volume corresponding to unrealistic intrusion (Sondergeld et al. 2010). Figure 3 shows the corrected measurements used to determine the pore-throat size distribution in this study.

Nitrogen adsorption

This study determined the pore-body size distributions of Samples 9–14 using nitrogen adsorption. Samples 9–14 were 0.9544, 0.7393, 0.9893, 0.5708, 0.7363, and 0.4717 g, respectively. Examples of the samples preheated and degassed for five hours at 300 °C to remove moisture are shown in Fig. 1. These samples were then cooled to reach room temperature. Subsequently, they were subjected to nitrogen adsorption at − 196 oC, which is the temperature at which nitrogen becomes liquid at the atmospheric pressure. This study did not account for the effects of sample size (Han et al. 2016; Chen et al. 2015; Hazra et al. 2018a, b) and degassing time and duration (Singh et al. 2021) on the pore-body size distribution because characterizing such effects is beyond the scope of this analysis.

The adsorptions were conducted under equilibrium conditions. At least a few data points were collected at each pressure increment with an equilibration time of 10 s. The

Fig. 3 Capillary pressure measurements of the shale samples
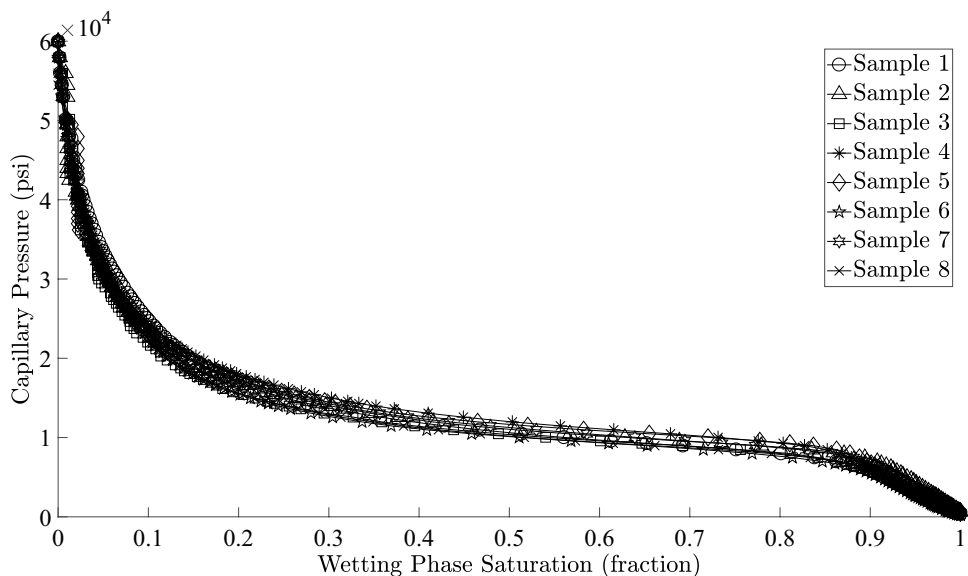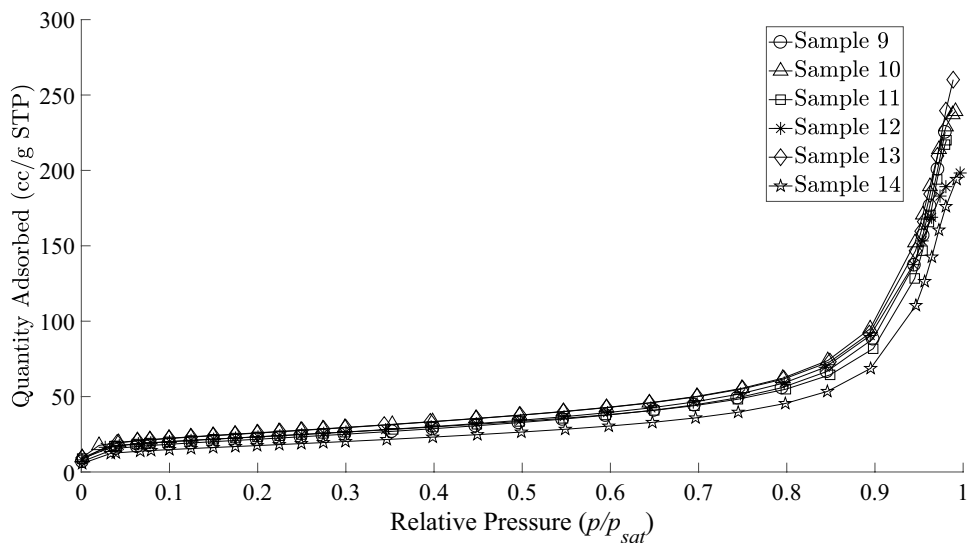

Fig. 4 Nitrogen adsorption measurements of the shale samples

adsorption lasted two to three hours for each sample to record 31–34 increments. Subsequently, the adsorbed volume was measured and normalized at each increment. The equilibrated nitrogen pressure (p) was then determined relative to the saturation pressure (p_{sat}) as shown in Fig. 4.

The pore-body size distribution was interpreted by the Barrett–Joyner–Halenda (BJH) model (Barrett et al. 1951) that is based on the Kelvin equation. The Kelvin equation relates the pore size to the saturation pressure, at which vapor turns into liquid, as follows (Fisher et al. 1981):

$$\mathrm{Ln}\left(\frac{p_v}{p_{sat}}\right) = -\frac{2H\gamma V_1}{RT} \tag{7}$$

where p_v is the vapor pressure, p_{sat} is the saturation pressure, H is the mean curvature of the meniscus, γ is the liquid–vapor surface tension, V_1 is liquid-molar volume, R is the ideal gas constant, and T is the temperature. The BJH model also accounts for the thickness (t) of the adsorbed nitrogen that depends on the pressure as follows (Harkins and Jura 1944):

$$t = \left[\frac{13.99}{0.034 - \log\left(\frac{p}{p_{sat}}\right)} \right]^{0.5} \tag{8}$$

The BJH model divides the adsorbed volume into pore filling by condensation (Eq. 7) and adsorbed-layer thickening on the pore wall (Eq. 8). The first mechanism leads to a sudden shift, whereas the latter causes a gradual increase in the adsorbed volume. The BJH compares the measured volume for a given pressure with the characteristic features of each size (sudden shift versus gradual increase) to determine the corresponding volume fraction. The conduit is assumed to be cylindrical to relate its diameter to volume.

Effective properties at the core scale

The pore-throat size and pore-body size distributions are determined from mercury injection capillary pressure measurements and nitrogen adsorptions, respectively. The pore-throat size was obtained from the applied capillary pressure using Eq. 5, and its frequency was obtained from the corresponding change in the wetting phase saturation (Fig. 3). Figure 5 shows the pore-throat size distributions show a wide range from 3 to 850 nm, with 94% of the pore throats smaller than 50 nm. Close to half the sizes are between 11 and 20 nm.

Discussed next are the pore-body size distributions. The adsorption measurements characterize the incremental volume of each pore-body size based on the BJH model. The incremental volumes were then divided by the total volume

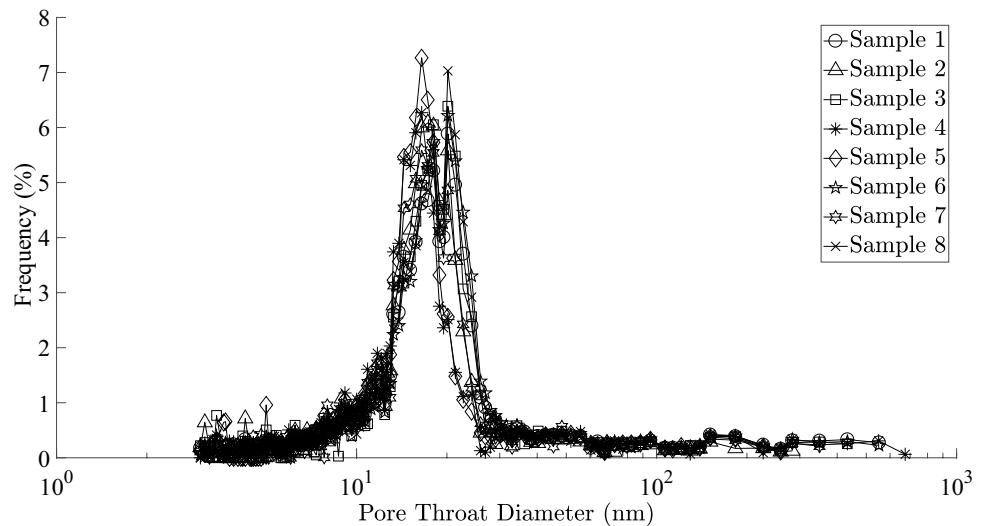**Fig. 5** Pore-throat size distributions of the shale samples

Fig. 6 Pore-body size distributions of the shale samples
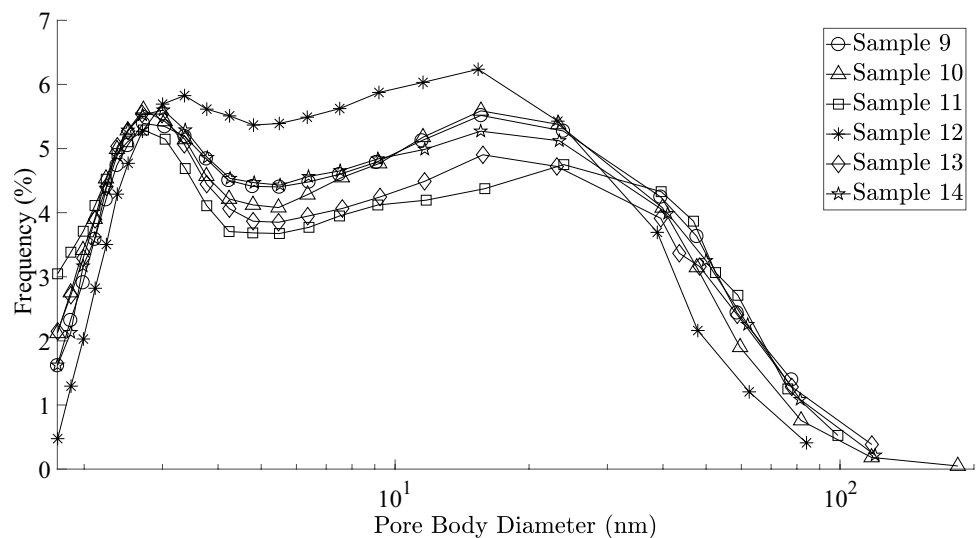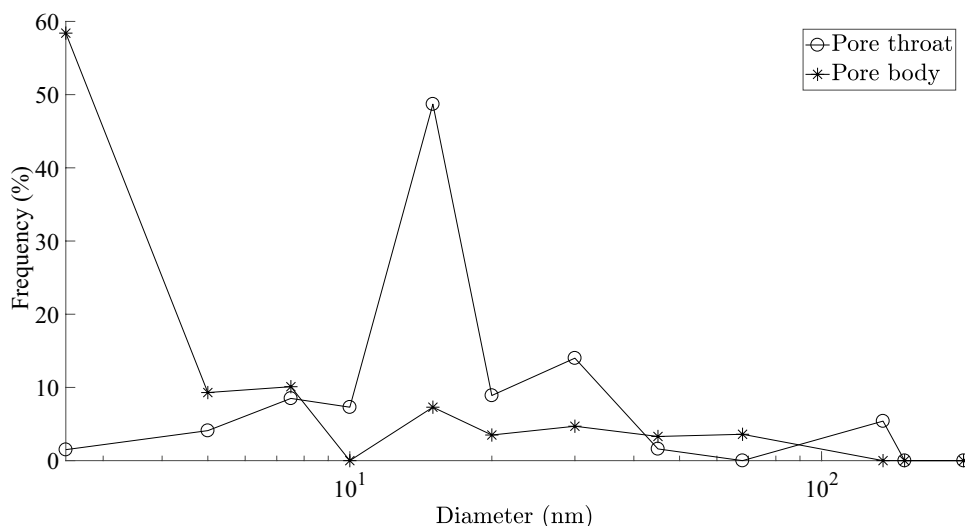
Fig. 7 Effective distributions of the shale based on the mercury injection capillary pressure measurements (Fig. 3) and nitrogen adsorptions (Fig. 4)

to determine the frequency of each size. Figure 6 shows that the distributions are bimodal, and the pore-body sizes vary from 1 to 200 nm.

Rock samples are heterogeneous, and that is why the two types of distributions are quite different. Thus, the distributions of each type were averaged to determine the effective sizes by accounting for the corresponding frequencies (Fig. 7). The effective frequencies of the pore-throat size distributions include eight samples (Fig. 5), whereas they reflect six samples in the pore-body size distributions (Fig. 6). The averaged distribution is considered effective at the core scale in this study.
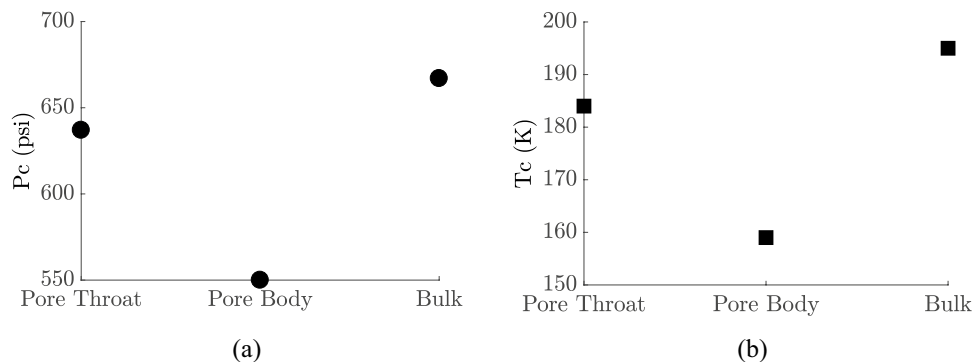
The pore-body size distribution includes smaller sizes than does the pore-throat size distribution. This difference is due to the measurements used for interpreting them. The mercury injection characterizes sizes down to 3 nm because the capillary pressure increased to 60,000 psi. However, nitrogen adsorption has limitations in detecting conduits wider than 200 nm, and it is better suited for characterizing nanosize pores (Liu et al. 2019; Yuan and Rezaee 2019). Thus, the pore-body distribution has a larger fraction of voids with a smaller size than the pore-throat distribution in Fig. 7.

Critical properties of the shale

Here, the actual critical properties of the Midra shale are discussed. The overestimations of the actual properties of each component by the bulk properties are determined by accounting for the frequencies of the effective distributions. The overestimation at each size is quantified via Eq. 3 and related to the core scale by accounting for its frequency (Fig. 7). This process is iterated for all components in Table 1 and averaged by accounting for their volume fraction in the mixture. The bulk properties overestimate the critical properties by 5% based on the pore-throat size distribution and 22% based on the pore-body size distribution. The determined overestimations specify the critical pressure (Fig. 8a) and critical temperature (Fig. 8b) corresponding to the pore throat and pore body. The bulk properties are also presented in Fig. 8 for comparison.

Fig. 8 **a** Critical pressure and **b** critical temperature of the studied shale

(a)

(b)

Sensitivity analysis

This study used actual measurements to determine the pore-throat size and pore-body size distributions, but it took the gas composition of the Midra shale similar to the shale gas in the USA because its gas composition is not currently available. Using the actual composition, when it becomes available, may improve the accuracy of the results.

In the literature, different values are reported for the Lennard–Jones coefficient (σ) of the gas component. For instance, for methane, it is reported to be 0.374 nm (Tchouar et al. 2003), 0.372 nm (Li et al. 2012), and 0.376 nm (Smoot, 1979). This study set the coefficient equal to 0.374 nm for methane, but different values do not change the estimated property significantly. The highest and lowest values for all the considered components in Table 1 change the estimated property between 0.4 and 0.2%.

Conclusions

We made the following conclusions based on this study:

(1) Bulk critical properties from standard measurements overestimate critical pressure and critical temperature in the shale matrix (actual properties), and the overestimation decreases when gas molecules are smaller.

(2) For the studied gas components, the overestimation varies between 15 and 26% in a 5 nm conduit and between 28 and 48% in a 3 nm conduit.

(3) The bulk properties overestimate the actual properties in Midra shale by 5% based on the pore-throat size distribution, interpreted from mercury injection, and 22% based on the pore-body size distribution, obtained from nitrogen adsorption.

(4) The actual properties depend on the Lennard–Jones coefficient that often has different values for each gas component in the literature. The actual properties changed by less than 1% for the existing values in Midra shale.

Declarations

References

Alessa S, Sakhaee-Pour A, Sadooni FN, Al-Kuwari HA (2021) Comprehensive pore size characterization of Midra shale. J Petrol Sci Eng 203:108576. https://doi.org/10.1016/j.petrol.2021.108576

Alessa S, Sakhaee-Pour A, Sadooni FN, Al-Kuwari HA (2022) Capillary pressure correction of cuttings. J Petrol Sci Eng 217:110908. https://doi.org/10.1016/j.petrol.2022.110908

Al-Saad H (2005) Lithostratigraphy of the middle eocene dammam formation in Qatar, Arabian Gulf: effects of sea-level fluctuations along a tidal environment. J Asian Earth Sci 25(5):781–789. https://doi.org/10.1016/j.jseaes.2004.07.009

Al-Saad H, Sadooni F (2011) Stratigraphy, facies analysis and reservoir characterization of the Upper Jurassic Arab C Qatar Arabian Gulf. Neues Jahrb für Geol Paläont Abh. https://doi.org/10.1127/0077-7749/2011/0205

Al-Saad H, Al-Khafaji AJ, Sadooni FN (2019) Evaluation of the source rock potential of the Unyazah formation (late carboniferous-early permian) in Dukhan Field. Qatar Pet Sci Technol 37(14):1655–1664. https://doi.org/10.1080/10916466.2019.1602636

Al-Shamali A, Mishra PK, Verma NK, Quttainah R, Al Jallad O, Grader A, Walls J, Koronfol S, Morcote A (2017) High-resolution porosity-permeability logs driven by macro-to-nano structures and PVT-pyro-geochemistry in a middle east unconventional formation. In: Abu Dhabi International Petroleum Exhibition and Conference (p. D021S053R003). SPE. doi: https://doi.org/10.2118/188230-MS

Al-Shawaf A, Al-Momen M, Issaka MB, Filipi I, Lewis C (2016) PTA and well performance assessment of dry and liquid rich gas in unconventional tight sands: a middle east case study. In: Abu Dhabi International Petroleum Exhibition and Conference (D031S058R001). SPE. https://doi.org/10.2118/183163-MS

Aruah B, Sakhaee-Pour A, Hatzignatiou DG, Sadooni FN, Al-Kuwari HA (2024) Altering shale permeability by cold shock. Gas Sci Eng 125:205291. https://doi.org/10.1016/j.jgsce.2024.205291

Bai J, Kang Y, Chen M, Liang L, You L, Li X (2019) Investigation of multi-gas transport behavior in shales via a pressure pulse method. Chem Eng J 360:1667–1677. https://doi.org/10.1016/j.cej.2018.10.197

Barrett Elliott P, Joyner Leslie G, Halenda Paul P (1951) The determination of pore volume and area distributions in porous substances. I. Computations from nitrogen isotherms. J Am Chem Soc 73(1):373–380. https://doi.org/10.1021/ja01145a126

Casey M, Rajan S, Kohshour IO, Adejumo A, Kugler I (2015) An economic model for field-wide shale gas development in Saudi

Arabia. In: SPE Middle East Unconventional Resources Conference and Exhibition (D031S011R001). SPE. doi: https://doi.org/10.2118/172954-MS

Cavelier C (1970) Geological description of the Qatar Peninsula. Bureau de recherches géologiques et minières

Chandra D, Bakshi T, Bahadur J, Hazra B, Vishal V, Kumar S, Singh TN (2023) Pore morphology in thermally-treated shales and its implication on CO2 storage applications: a gas sorption, SEM, and small-angle scattering study. Fuel 331:125877. https://doi.org/10.1016/j.fuel.2022.125877

Chen Y, Wei L, Mastalerz M, Schimmelmann A (2015) The effect of analytical particle size on gas adsorption porosimetry of shale. Int J Coal Geol 138:103–112. https://doi.org/10.1016/j.coal.2014.12.012

Clarkson CR, Solano N, Bustin RM, Bustin AMM, Chalmers GR, He L, Melnichenko YB, Radlinski AP, Blach TP (2013) Pore structure characterization of North American shale gas reservoirs using USANS/SANS, gas adsorption, and mercury intrusion. Fuel 103:606–616. https://doi.org/10.1016/j.fuel.2012.06.119

Deng H, Hu X, Li HA, Luo B, Wang W (2016) Improved pore-structure characterization in shale formations with FESEM technique. J Natur Gas Sci Eng 35:309–319. https://doi.org/10.1016/j.jngse.2016.08.063

Eijkel JC, Berg AVD (2005) Nanofluidics: what is it and what can we expect from it? Microfluid Nanofluid 1:249–267. https://doi.org/10.1007/s10404-004-0012-9

Fisher LR, Gamble RA, Middlehurst J (1981) The Kelvin equation and the capillary condensation of water. Nature 290(5807):575–576. https://doi.org/10.1038/290575a0

Han H, Cao Y, Chen SJ, Lu JG, Huang CX, Zhu HH, Gao Y (2016) Influence of particle size on gas-adsorption experiments of shales: An example from a Longmaxi Shale sample from the Sichuan Basin, China. Fuel 186:750–757. https://doi.org/10.1016/j.fuel.2016.09.018

Harkins William D, Jura George (1944) Surfaces of solids. XIII. A vapor adsorption method for the determination of the area of a solid without the assumption of a molecular area, and the areas occupied by nitrogen and other molecules on the surface of a solid. J Am Chem Soc 66(8):1366–1373. https://doi.org/10.1021/ja01236a048

Hazra B, Wood DA, Vishal V, Singh AK (2018a) Pore characteristics of distinct thermally mature shales: influence of particle size on low-pressure CO2 and N2 adsorption. Energy Fuels 32(8):8175–8186. https://doi.org/10.1021/acs.energyfuels.8b01439

Hazra B, Wood DA, Vishal V, Varma AK, Sakha D, Singh AK (2018b) Porosity controls and fractal disposition of organic-rich Permian shales using low-pressure adsorption techniques. Fuel 220:837–848

Hazra B, Chandra D, Lahiri S, Vishal V, Sethi C, Pandey JK (2023) Pore evolution during combustion of distinct thermally mature shales: insights into potential in situ conversion. Energy Fuels 37(18):13898–13911. https://doi.org/10.1021/acs.energyfuels.3c02320

Huy Tran A, Sakhaee-Pour, (2019) The compressibility factor (Z) of shale gas at the core scale. Petrophys SPWLA J Form Eval Reserv Descrip 60(4):494–506. https://doi.org/10.30632/PJV60N4-2019a3

Jia B, Tsau JS, Barati R (2019) A review of the current progress of CO2 injection EOR and carbon storage in shale oil reservoirs. Fuel 236:404–427. https://doi.org/10.1016/j.fuel.2018.08.103

Jin L, Ma Y, Jamili A (2013) Investigating the effect of pore proximity on phase behavior and fluid properties in shale formations. In: SPE Annual Technical Conference and Exhibition. OnePetro. doi: https://doi.org/10.2118/166192-MS

Jin Z, Firoozabadi A (2016) Thermodynamic modeling of phase behavior in shale media. SPE J 21(01):190–207. https://doi.org/10.2118/176015-PA

Korpys M, Wojcik J, Synowiec P (2014) Methods for sweetening natural and shale gas. Chem Sci 68(3):213–215

Li Y, Yu Y, Zheng Y, Li J (2012) Vapor-liquid equilibrium properties for confined binary mixtures involving CO 2, CH 4, and N 2 from Gibbs ensemble Monte Carlo simulations. Sci China Chem 55:1825–1831. https://doi.org/10.1007/s11426-012-4724-5

Li ZZ, Min T, Kang Q, He YL, Tao WQ (2016) Investigation of methane adsorption and its effect on gas transport in shale matrix through microscale and mesoscale simulations. Int J Heat Mass Transf 98:675–686. https://doi.org/10.1016/j.ijheatmasstransfer.2016.03.039

Liu Kouqi, Ostadhassan Mehdi, Cai Jianchao (2019) Characterizing pore size distributions of shale. Petrophysical characterization and fluids transport in unconventional reservoirs. Elsevier, pp 3–20. https://doi.org/10.1016/B978-0-12-816698-7.00001-2

Liu L, Nieto-Draghi C, Lachet V, Heidaryan E, Aryana SA (2022) Bridging confined phase behavior of CH4-CO2 binary systems across scales. J Supercrit Fluids 189:105713. https://doi.org/10.1016/j.supflu.2022.105713

Loucks RG, Reed RM, Ruppel SC, Jarvie DM (2009) Morphology, genesis, and distribution of nanometer-scale pores in siliceous mudstones of the Mississippian Barnett Shale. J Sediment Res 79(12):848–861. https://doi.org/10.2110/jsr.2009.092

Ma Y, Jin L, Jamili A (2013) Modifying van der Waals equation of state to consider influence of confinement on phase behavior. In: SPE Annual Technical Conference and Exhibition? (D031S051R007). SPE. doi: https://doi.org/10.2118/166476-MS

Mastalerz M, Schimmelmann A, Drobniak A, Chen Y (2013) Porosity of devonian and mississippian new albany shale across a maturation gradient: insights from organic petrology, gas adsorption, and mercury intrusion. AAPG Bull 97(10):1621–1643. https://doi.org/10.1306/04011312194

Milliken KL, Rudnicki M, Awwiller DN, Zhang T (2013) Organic matter–hosted pore system, Marcellus formation (Devonian). Pa AAPG Bulletin 97(2):177–200. https://doi.org/10.1306/07231212048

Pratt DT, Smoot L, Pratt D (1979) Pulverized coal combustion and gasification. Springer, Berlin. https://doi.org/10.1007/978-1-4757-1696-2

Sahin A (2013) Unconventional natural gas potential in Saudi Arabia. In: SPE Middle East Oil and Gas Show and Conference. OnePetro. doi: https://doi.org/10.2118/164364-MS

Sakhaee-Pour A, Bryant SL (2012) Gas permeability of shale. SPE Reservoir Eval Eng 15(04):401–409. https://doi.org/10.2118/146944-PA

Sakhaee-Pour A, Bryant SL (2015) Pore structure of shale. Fuel 143:467–475. https://doi.org/10.1016/j.fuel.2014.11.053

Sakhaee-Pour A, Li W (2016) Fractal dimensions of shale. J Natur Gas Sci Eng 30:578–582. https://doi.org/10.1016/j.jngse.2016.02.044

Singh SK, Singh JK (2011) Effect of pore morphology on vapor–liquid phase transition and crossover behavior of critical properties from 3D to 2D. Fluid Phase Equilib 300(1–2):182–187. https://doi.org/10.1016/j.fluid.2010.10.0145

Singh DP, Chandra D, Vishal V, Hazra B, Sarkar P (2021) Impact of degassing time and temperature on the estimation of pore attributes in shale. Energy Fuels 35(19):15628–15641. https://doi.org/10.1021/acs.energyfuels.1c02201

Sondergeld CH, Newsham KE, Comisky JT, Rice MC, Rai CS (2010) Petrophysical considerations in evaluating and producing shale gas resources. In: SPE unconventional gas conference. OnePetro. doi: https://doi.org/10.2118/131768-MS

Song W, Yao J, Li Y, Sun H, Yang Y (2018) Fractal models for gas slippage factor in porous media considering second-order slip and

surface adsorption. Int J Heat Mass Transf 118:948–960. https://doi.org/10.1016/j.ijheatmasstransfer.2017.11.072

Taghavinejad A, Sharifi M, Heidaryan E, Liu K, Ostadhassan M (2020) Flow modeling in shale gas reservoirs: A comprehensive review. J Natur Gas Sci Eng 83:103535. https://doi.org/10.1016/j.jngse.2020.103535

Tchouar N, Benyettou M, Kadour F (2003) Thermodynamic, structural and transport properties of Lennard-Jones liquid systems. A molecular dynamics simulations of liquid helium, neon, methane and nitrogen. Int J Molecul Sci 4(12):595–606. https://doi.org/10.3390/i4120595

Teklu TW, Alharthy N, Kazemi H, Yin X, Graves RM, AlSumaiti AM (2014) Phase behavior and minimum miscibility pressure in nanopores. SPE Reservoir Eval Eng 17(03):396–403. https://doi.org/10.2118/168865-PA

Tran H, Sakhaee-Pour A (2018) Critical properties (Tc, Pc) of shale gas at the core scale. Int J Heat Mass Transf 127:579–588. https://doi.org/10.1016/j.ijheatmasstransfer.2018.08.054

Wang S, Javadpour F, Feng Q (2016) Fast mass transport of oil and supercritical carbon dioxide through organic nanopores in shale. Fuel 181:741–758. https://doi.org/10.1016/j.fuel.2016.05.057

Wang J, Yuan Q, Dong M, Cai J, Yu L (2017) Experimental investigation of gas mass transport and diffusion coefficients in porous media with nanopores. Int J Heat Mass Transf 115:566–579. https://doi.org/10.1016/j.ijheatmasstransfer.2017.08.057

Xiong W, Zhao YL, Qin JH, Huang SL, Zhang LH (2021) Phase equilibrium modeling for confined fluids in nanopores using an association equation of state. J Supercrit Fluids 169:105118. https://doi.org/10.1016/j.supflu.2020.105118

Yu C, Tran H, Sakhaee-Pour A (2018) Pore size of shale based on acyclic pore model. Transp Porous Media 124:345–368. https://doi.org/10.1007/s11242-018-1068-4

Yuan Y, Rezaee R (2019) Comparative porosity and pore structure assessment in shales: measurement techniques, influencing factors and implications for reservoir characterization. Energies 12(11):2094. https://doi.org/10.3390/en12112094

Zarragoicoechea GJ, Kuz VA (2002) van der Waals equation of state for a fluid in a nanopore. Phys Rev E 65(2):021110. https://doi.org/10.1103/PhysRevE.65.021110

Zarragoicoechea GJ, Kuz VA (2004) Critical shift of a confined fluid in a nanopore. Fluid Phase Equilib 220(1):7–9. https://doi.org/10.1016/j.fluid.2004.02.014

Zhao YL, Xiong W, Zhang LH, Qin JH, Huang SL, Guo JJ, He X, Wu JF (2021) Phase equilibrium modeling for interfacial tension of confined fluids in nanopores using an association equation of state. J Supercrit Fluids 176:105322. https://doi.org/10.1016/j.supflu.2021.105322